12th ANKARA INTERNATIONAL AEROSPACE CONFERENCE AIAC-2023-073
13-15 September 2023 - Online, Ankara, TURKIYE

ESTIMATION OF WAKE INDUCED POWER LOSSES IN A LARGE OFFSHORE WIND FARM USING ACTUATOR DISK AND LES MODELS

Huseyin C. Onel* and Ismail H. Tuncer†
Middle East Technical University
Ankara, Turkey

ABSTRACT

Numerical wind farm simulations are challenging due to the wide range of length and time scales. Actuator models provide a great trade-off between fidelity and computational cost for the simulation of wind turbines rotors in micro-scale numerical atmospheric flow solutions. In this study, large eddy simulation of a large offshore wind farm that consists of 48 wind turbines is conducted with OpenFOAM under unidirectional flow conditions. Inflow is generated as an ideal atmospheric boundary layer profile. Rotors are modeled as advanced rotating actuator disks, where rotor pitch, speed and yaw is automatically controlled dynamically. Equivalent blade and rotors are designed to resemble the turbines utilized in the wind farm, whose details are not available due to commercial purposes. Wake structures are captured physically. Wake-induced power losses are evaluated under the axially-aligned configuration and the results are found to be in alignment with the field measurements.

INTRODUCTION

The growth of wind energy is evident as electricity generation from wind surged by 265 TWh (14%) in 2022, surpassing a total of 2100 TWh [Internatonal Energy Agency, 2023]. The increasing use of wind energy has led to a rise in offshore wind farms, where turbines are clustered for cost optimization. However, this clustering causes performance reductions due to wake losses caused by turbine interactions. Wind speed reduction downstream of turbines results in power losses. The intensity of these losses depends on turbine spacing, with closer spacing leading to higher wake losses. Estimating wake losses and global blockage is essential for designing wind farms and calculating energy production and revenues [Barthelmie et al., 2011].

Various numerical models and software tools with different levels of accuracy and computational costs can perform these calculations. Operating data from SCADA systems are commonly analyzed to evaluate wind farm performance, including wake effects and global blockage. Modeling of wake turbulence can lead to significant improvements in wind farm design and operation. Although power curve based approaches are simple and low-cost [Sohoni et al., 2016], they lack high fidelity wake dynamics. On the other extreme, utilizing a fully-resolved blade geometry in a wind farm simulation is

*Research Assistant in the Department of Aerospace Engineering, e-mail: canon@metu.edu.tr
†Professor in the Department of Aerospace Engineering, e-mail: ismail.h.tuncer@ae.metu.edu.tr

extremely expensive [qi Wang et al., 2018]. Actuator models offer a good trade-off in the middle. The Actuator Line Model (ALM) yields a better representation of the flow by resolving the tip vortices with higher accuracy [Sørensen and Shen, 2002], but needs a fine grid resolution and smaller timesteps. The Actuator Disk Model (ADM) is less expensive at the cost of some level of fidelity, yet both of its simple [Porté-Agel et al., 2011; Olivares-Espinosa et al., 2014] and advanced [Wu and Porté-Agel, 2011; Martínez-Tossas et al., 2022] variations are still used extensively by wind energy researchers.

Turbine wakes are highly turbulent structures. Hence, the turbulence model also plays an important role. Reynolds-Averaged Navier-Stokes (RANS) models are inexpensive and easy to implement. Atmospheric turbulence can be easily adjusted and controlled [Tabib et al., 2015; Van Der Laan et al., 2015]. Large Eddy Simulation (LES) yields higher fidelity flow fields, but requires a much finer grid resolution and small timestep, hence higher computational resources. It also requires special methods to generate atmospheric turbulence, such as precursor [Churchfield et al., 2012; Stevens et al., 2018] or synthetic [Ivanell et al., 2007; Nilsson et al., 2015] models.

In this study, the Lillgrund offshore wind farm is simulation under unidirectional flow conditions. OpenFOAM is used for the Large Eddy Simulation (LES) flow solutions. Inflow atmospheric boundary layer is imposed as an ideal logarithmic profile. Turbines are modeled with an improved Rotating Actuator Disk Model (ADM-R), in which autonomous controller capabilities are integrated. The Siemens wind turbines utilized in the wind farms has no detailed blade and rotor data available, hence an equivalent turbine is designed using the Blade Element Momentum (BEM) method and used in the simulations. Energy production of the turbines and wake-induced power losses are calculated and discussed, which are found to be in line with the field measurements.

METHOD

In the present study, the wind farm simulation is based on numerical methods and models. The flow is solved using the open-source OpenFOAM [Weller et al., 1998]. The open-source Blade Element Momentum (BEM) solver, QBlade [Marten and Wendler, 2013], is used for the blade and rotor design. Turbines are modeled as rotating actuator disks as proposed by [Wu and Porté-Agel, 2011], with some modifications. Details of the methodology is given in this section.

Flow Solver: OpenFOAM

OpenFOAM is a finite volume based CFD toolbox which offers ease of code modification. Flow is assumed incompressible, and solved under unsteady regime. Turbulence is modeled with the Large Eddy Simulation (LES) approach. The governing equations for a filtered (resolved) quantity $\langle\Phi\rangle$ are mass and momentum conservation:

$$\frac{\partial\langle u_i\rangle}{\partial x_i} = 0 \tag{1}$$

$$\frac{\partial\langle u_i\rangle}{\partial t} + \frac{\partial\langle u_i u_j\rangle}{\partial x_j} = -\frac{1}{\partial\rho}\frac{\partial\langle p\rangle}{\partial x_i} + \nu\left(\frac{\partial\langle u_i\rangle}{\partial x_j} + \frac{\partial\langle u_j\rangle}{\partial x_i}\right) + f_i \tag{2}$$

The nonlinear $\langle u_i u_j\rangle$ term is approximated using the following approximation:

$$\tau_{ij}^r = \rho\left(\langle u_i\rangle\langle u_j\rangle - \langle u_i u_j\rangle\right) \tag{3}$$

where τ_{ij}^r is the *sub-grid scale residual stress*, and it is modeled using the Smagorinsky [SMAGORINSKY, 1963] model:

$$\tau_{ij}^r - \frac{1}{3}\tau_{kk}^r\delta_{ij} = 2\mu_t\langle S_{ij}\rangle \tag{4}$$

Here, μ_t is the eddy viscosity and $\langle S_{ij}\rangle$ is the rate of strain of the filtered variables. The eddy viscosity is given as:

$$\mu_t = \rho C_s^2\Delta^2\sqrt{(\langle S_{ij}\rangle\langle S_{ij}\rangle)} \tag{5}$$

where $C_s = 0.168$ is the Smagorinsky coefficient and Δ represents a filter length, taken as the cube-root of the cell volume. The pressure-velocity decoupling is handled through the PISO algorithm [Issa, 1986].

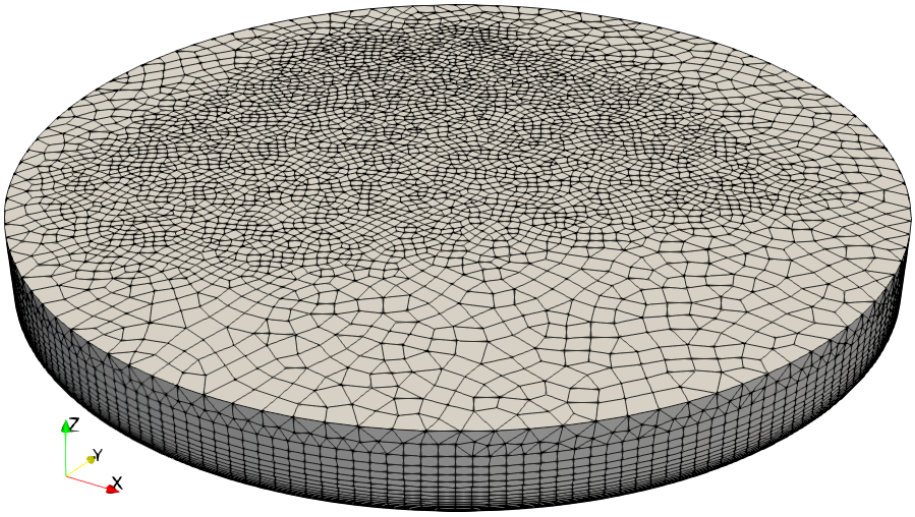

Figure 1: OpenFOAM solution grid

A cylindrical solution grid is utilized (Fig. 1). It is a hybrid mesh, consisting of tetra, pyramid, prism and hexa cells. The open-source GMSH code [Geuzaine and Remacle, 2009] is used for mesh generation. A modified freestream type BC is applied at the farfield, which switches to Dirichlet and Neumann conditions at the inlet and outlet cells, respectively.

At the inlet, idealized logarithmic ABL velocity profile (Eq. (6)) is imposed as proposed by [Hargreaves and Wright, 2007]. Zero-gradient velocity is applied at the outlet. Slip boundary conditions are applied at the top plane. At the wall, surface roughness is set to $z_0 = 5 \times 10^{-4}$ which represents *blown sea*. Eddy viscosity is adjusted to ensure Spalding's law of the wall, maintaining the ABL profile.

$$|\mathbf{u}|(z) = \frac{u^*}{\kappa} \ln\left(\frac{z - z_d + z_0}{z_0}\right) \tag{6}$$

$$u^* = \frac{u_{\text{ref}}\kappa}{\ln\left(\frac{z_{\text{ref}}+z_0}{z_0}\right)} \tag{7}$$

Second order schemes are used for time and space integration. Due to the PISO algorithm requirements, CFL number is limited by $\text{CFL}_{\max} = 1$. Solution is performed on 12 cores in parallel.

The Rotating Actuator Disk Model (ADM-R)

Among the two most popular actuator models, the Actuator Line model (ALM) requires a time step size small enough, such that the blade tip does not travel more than a grid cell in a single time step ($\text{CFL}_{\text{tip}} < 1$). The Actuator Disk Model (ADM) is free from this limitation, making it much more cost effective [Martínez et al., 2012]. Moreover, the rotating ADM (ADM-R) can capture swirling effects and yields accurate wake physics. Hence, ADM-R proposed by [Wu and Porté-Agel, 2011] is used in this study.

The ADM-R is methodologically similar to BEM. The rotor swept area is divided into equidistant *actuator points* (APs) as shown in Fig. 2. Lift and drag forces are calculated at each AP based on the 2D airfoil theory:

$$F_{L|D} = -\frac{1}{2}\rho U_{\text{rel.}}^2 c_{l|d} c_E S_E \tag{8}$$

Here, the axial component of the local velocity (U_n) is directly probed from the velocity field in ADM-R, unlike BEM (where it is calculated by induction factors). Aerodynamic coefficients (c_l c_d)

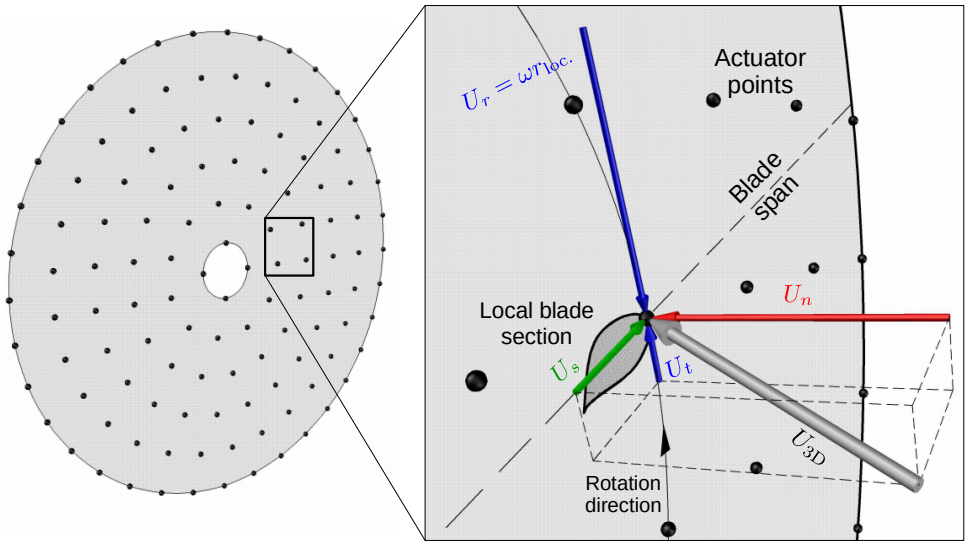

Figure 2: Schematic of the Rotating Actuator Disk Model (ADM-R)

are provided as pre-tabulated data, which are calculated using the XFOIL code developed by [Drela, 1989]. Hence, the detailed blade geometry, i.e. chord, twist and airfoil shape distribution, should be available beforehand. After calculating F_L and F_D, they are transformed into the rotor coordinate system, yielding axial and tangential components F_a and F_t, respectively. These forces are then projected onto the Navier-Stokes solution field as a momentum source field (i.e. f_i term in Eq. (2)). Instead of imposing the force to the nearest cell in a singular manner, projection is realized by $smearing$ the calculated force among the cells in the AP vicinity. This practice ensures a stable solution and prevents force-velocity decoupling. The projected force field deflects the velocity field, and in return, the new velocity field induces a new force field. Hence, an iterative process takes place between the force and velocity fields until convergence at each time step.

In the present study, the ADM-R code is based on the SOWFA library of OpenFOAM, developed by NREL [Churchfield, 2017]. The ADM-R part of the library is extracted and implemented into a standalone PIMPLE based solver. Moreover, the code is modified and autonomous controller parameters are integrated. This is achieved by each turbine reading pre-tabulated pitch and speed curves during run time and setting its rotor speed and blade pitch angle based on the local wind speed. Hence, turbines are capable of operating at their optimum power even when under the influence of wake, resembling a real-life wind turbine.

RESULTS AND DISCUSSION

The methodology is applied to the Lillgrund offshore wind farm. In this section, designation of the simulation site is explained first. Then, an equivalent wind turbine is designed. Details of the simulation setup is given, and the results are presented in terms of qualitative solution fields. Finally, relative power production of wind turbines are given, and the wake-induced power losses are discussed.

The Lillgrund Offshore Wind Farm

The Lillgrund wind farm is located about $10\ km$ off the coast of southern Sweden and has a capacity of $110MW$. Siemens SWT-2.3-93 machines are utilized, which yields $2.3\ MW$ of nominal power. Tower height is $65\ m$ from the sea surface to the rotor hub. The farm consists of 48 wind turbines. The arrangement can be described in 8 rows (A-H) and 8 columns (1-8) as shown in Fig. 3. Compared to the common practice, where turbines are separated by some distance of around 7 diameters, wind turbines are positioned relatively close to each other here. Separation distances are $4.3D$ and $3.3D$ in the row-wise and column-wise directions, respectively. The wind farm has been extensively studied by many wind energy researchers, thus there is a large body of data available. Accordingly, it is chosen

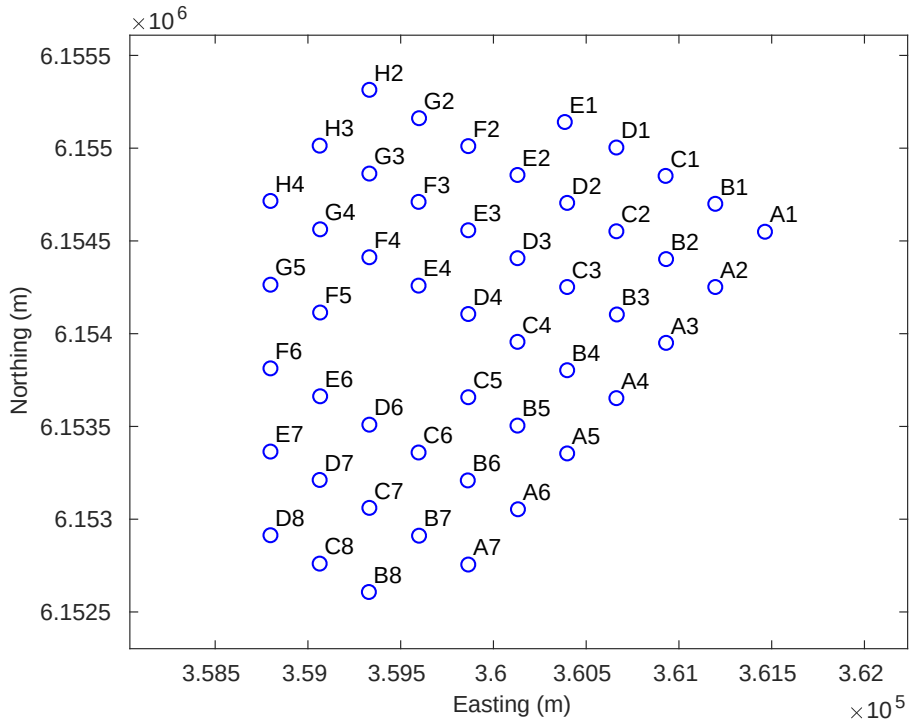

Figure 3: Turbine layout of the Lillgrund wind farm

as the simulation site.

Around the plant site, the dominant wind direction is reported to be westerly ($\approx 270^o$) by [Jeppsson et al., 2008]. In the case of a 222^o southwestern wind direction, each turbine row becomes axially-aligned. This setup provides an extreme wake-induced power loss scenario, which makes and interesting case study.

Equivalent Turbine Design

Unlike the uniformly distributed simple ADM, the rotating actuator disk model needs the detailed blade geometry and rotor parameters to operate. However, these data is almost never made available for commercial wind turbines by their manufacturers. Therefore, there was a need to design a turbine with equivalent characteristics.

Table 2: Specifications of the Siemens SWT-2.3-93 commercial wind turbine

Diameter	93 m
Number of blades	3
Rated power	2300 kW
Rated TSR	6
Rated wind speed	13 m/s
Cut-in wind speed	3.5 m/s
Cut-out wind speed	25 m/s
Min. rotor speed	6 min^{-1}
Max. rotor speed	16 min^{-1}
Tower height	65 m

Primary specifications of the Siemens SWT-2.3-93 wind turbine is given in Table 2. Based on this information, an equivalent blade is designed and its operation curves are determined. The simple yet proven Blade Element Momentum (BEM) theory is utilized for this purpose. The open-source BEM code QBlade [Marten and Wendler, 2013] is used for simulations.

Table 1: Blade geometry of the equivalent turbine

$r(m)$	$c(m)$	$\beta(^o)$	Airfoil section
1.11	2.150	72.88	Circular Foil $c_d = 0.50$
2.11	2.245	62.79	Circular Foil $c_d = 0.50$
4.13	2.438	46.36	Circular Foil $c_d = 0.50$
6.15	2.631	35.03	Circular Foil $c_d = 0.35$
8.67	2.872	21.79	DU99W405
11.70	3.161	13.83	DU99W350
14.73	3.450	9.33	DU99W350
17.75	3.160	3.23	DU97W300
20.78	2.870	1.96	DU91W2250
23.80	2.580	0.25	DU91W2250
26.83	2.290	-1.10	DU93W210
29.86	1.999	-2.18	DU93W210
32.88	1.709	-3.07	NACA64618
35.91	1.419	-3.81	NACA64618
38.93	1.129	-4.44	NACA64618
41.46	0.886	-4.90	NACA64618
43.47	0.694	-5.22	NACA64618
45.49	0.500	-5.52	NACA64618
46.50	0.250	-5.66	NACA64618

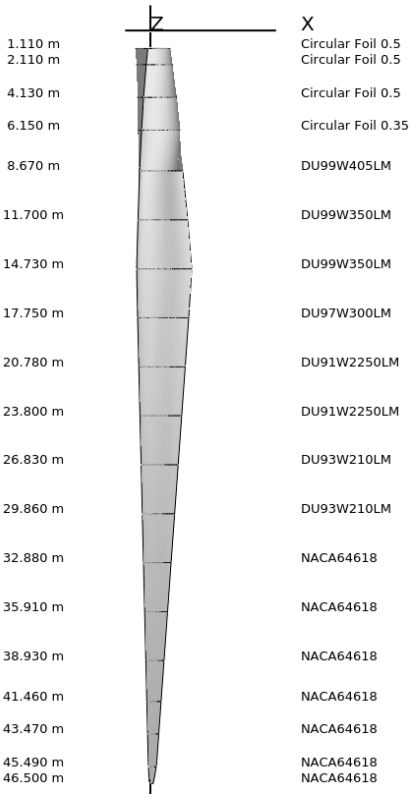

Figure 4: Blade geometry of the equivalent turbine

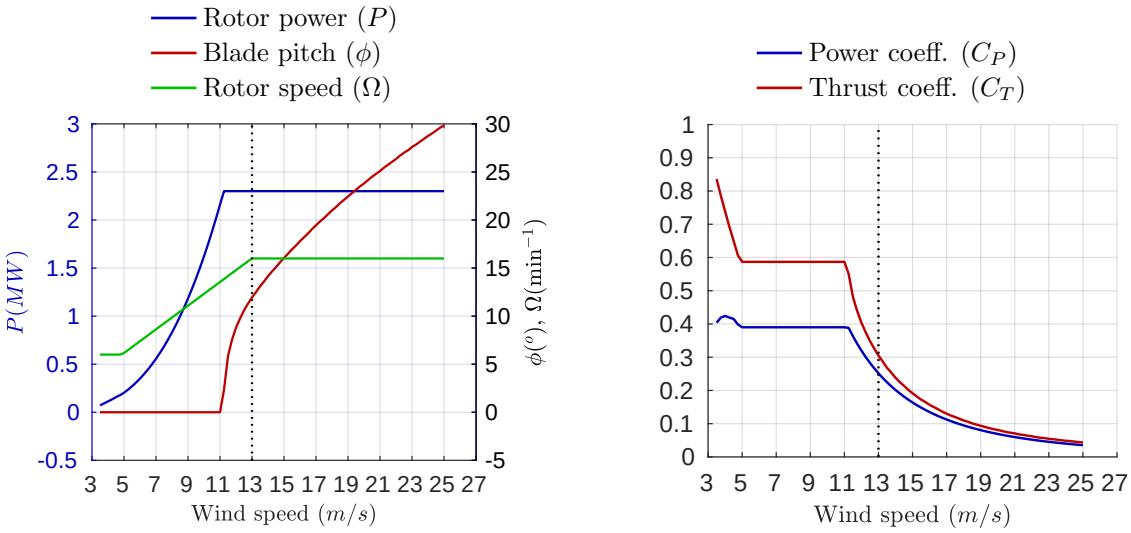

Figure 5: Characteristic curves of the equivalent turbine

The base geometry of the blade is obtained from the extensively used NREL-5MW [Jonkman et al., 2009]. First, the rotor radius and chord distribution are linearly downscaled by a factor of $93/126$. Then, the chord and twist distributions are optimized to yield the maximum power at the design tip speed ratio of TSR$= 6$ with the constraint of remaining in the $\pm 5\%$ of the maximum c_l/c_d ratio. The resulting chord and twist distributions and the corresponding airfoil sections are given in Table 1, and the 3D visualization of the blade is shown in Fig. 4.

After the blade design is completed, the rotor is analyzed for the full operational wind speed range

of $3.5 - 22\ m/s$. Here, the rated wind speed ($13\ m/s$), the rotor speed range of $6 - 16\ \mathrm{min}^{-1}$ and the generator capacity of $2.3\ MW$ are set as the design goals. The resulting power curve is shown in Fig. 5, as well as the variation of blade pitch and rotor speed with wind speed. Some maximum power coefficient of $C_P \approx 0.4$ could be achieved, which can be considered low for a commercial turbine. Also, the sharp variation in the pitch angle around $U_\infty \approx\ 11m/s$ is of significance. Yet, the current design is assumed sufficient for this study, considering the simplistic methodology of BEM.

OpenFOAM Simulation Setup

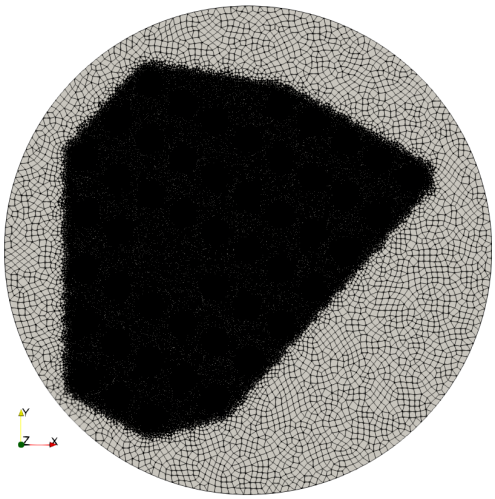

(a) Horizontal cut at the hub height (full view)

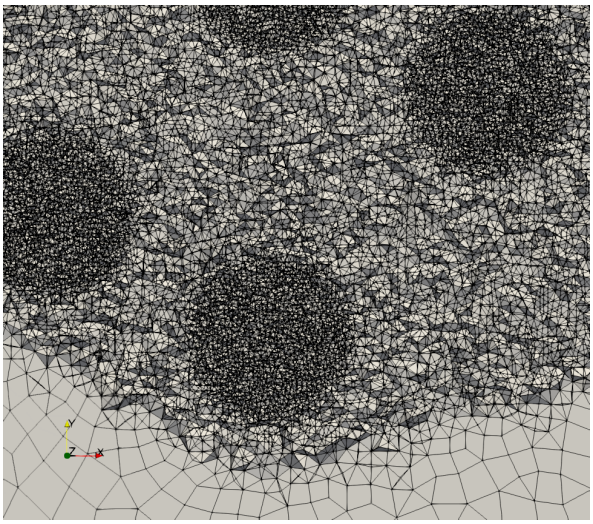

(b) Horizontal cut at the hub height (zoomed to turbine B8)

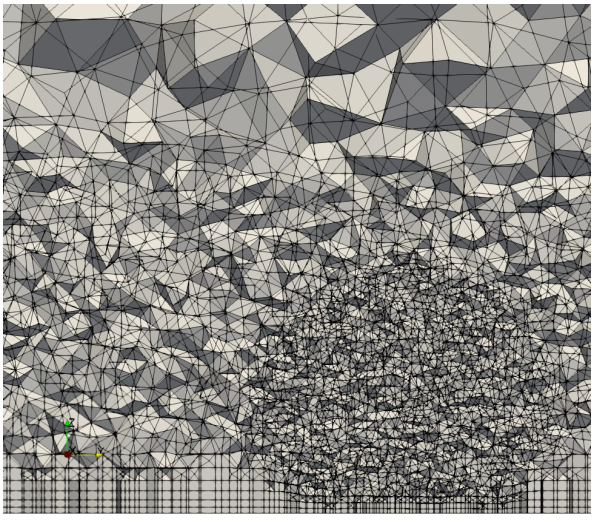

(c) Vertical cut passing through a rotor center (zoomed to turbine B6)

Figure 6: OpenFOAM solution grid generated for the Lillgrund wind farm simulations

The radius of the cylindrical OpenFOAM grid is determined according to the turbine layout. Center of the domain is set as the midpoint of the rectangle that circumscribes the outermost turbines (Fig. 6a). In that case, the farthest turbine to the domain center is D8. The farfield boundary is located $300\ m$ away from this turbine (approximately 3.2 diameters), thus the resulting domain radius is $\approx 2\ km$. Within the mesh block, refinement volumes are defined for rotor and wake regions as spheres and polygons, respectively. Cell size is on the order of 1 diameter at the farfield, which gradually decreases down to $1/8\ D$ ($\Delta_L = 11.6\ m$) at the wake region and $1/16\ D$ ($\Delta_L = 5.8\ m$) at the rotor region (Fig. 6b). At the wall, the wall-adjacent cell height is set $\Delta z_w = 4\ m$ and the cell aspect ratio is fixed

at 15. This layer is inflated with some 1.2 growth ratio, which blends into wake and rotor refinement regions (Fig. 6c). The resulting grid consists of about 10 million cells.

The freestream wind speed is set to constant $U_\infty = 8\ m/s$, which is the yearly average wind speed observed in the wind farm. Wind direction is kept constant at 222^o. 10 minutes of simulation time is run to obtain a completely statistically-steady flow field, where fully developed wake interactions are ensured between the farthermost turbines.

Wind Farm Simulation Results

First, the inner domain is initialized as a uniform flow field. Then, a solution is obtained for 10 minutes of simulation time without the rotors present to get a fully developed flow field, reflecting the atmospheric boundary layer. Following this, the turbines are introduced into the field, and the simulation is continued from the last time step of the previous simulation for another 10 minutes. Presented results are from this second run.

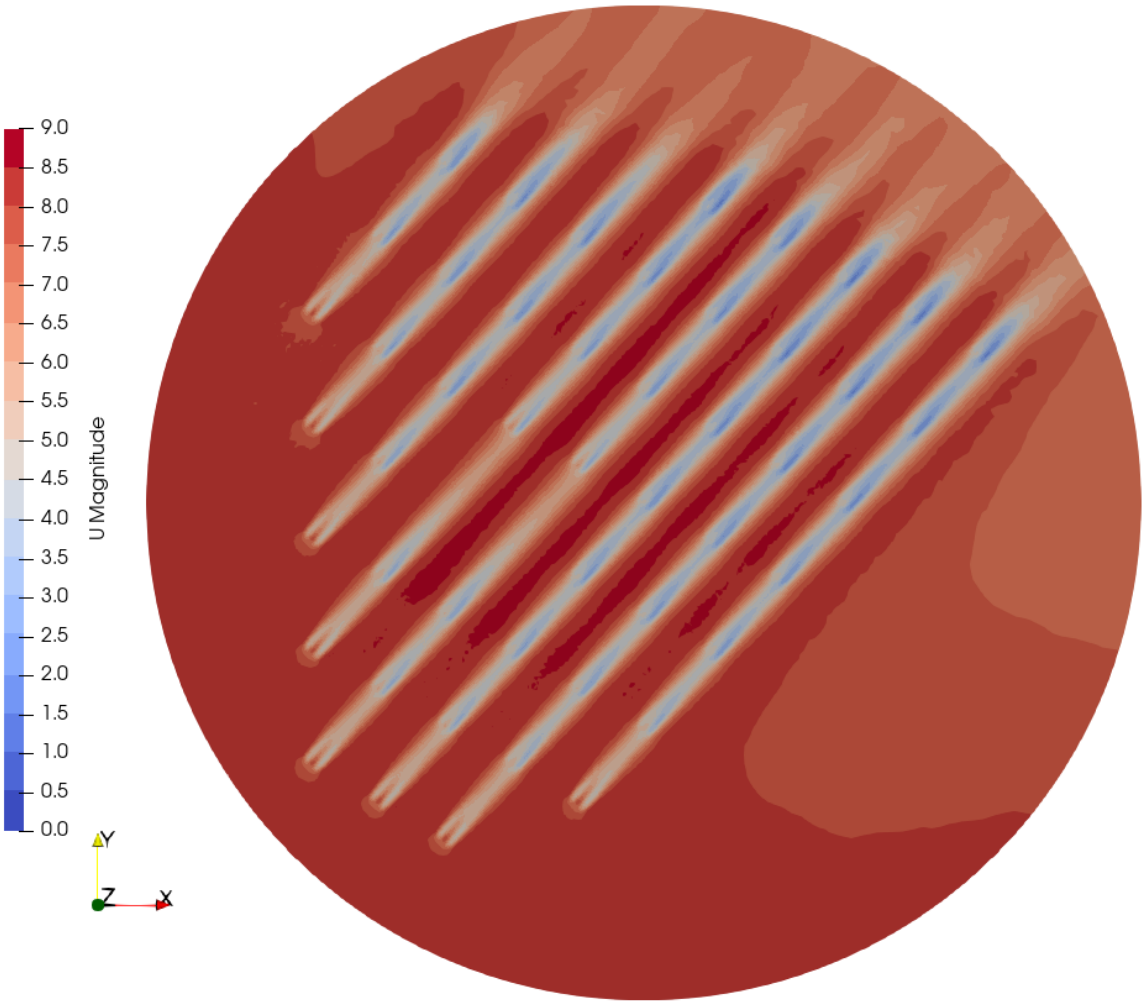

Figure 7: Instantaneous velocity magnitude contours at the rotor hub height ($z = 65\ m$)

Fig. 7 shows the velocity magnitude contours at the rotor hub height, respectively. A small low-speed region in front of the row-first turbines (A7, B8, C8, D8, E7, F6, G5 and H4) are visible, where the flow is retarded due to the induction effect by the rotors. The velocity deficit in the wake regions are also clearly visible. Slow-down of the flow is stronger behind the downstream turbines, compared to the row-first rotors. Behind the row-first rotors, wind speed drops to a minimum of $4.8\ m/s$ in the near-wake region (1-2 diameter), but recovers to $5.3\ m/s$ towards the the row-second turbines, around 3-4 diameter distance. Wind speed is further slowed down to $3.5\ m/s$ in the near-wake of the

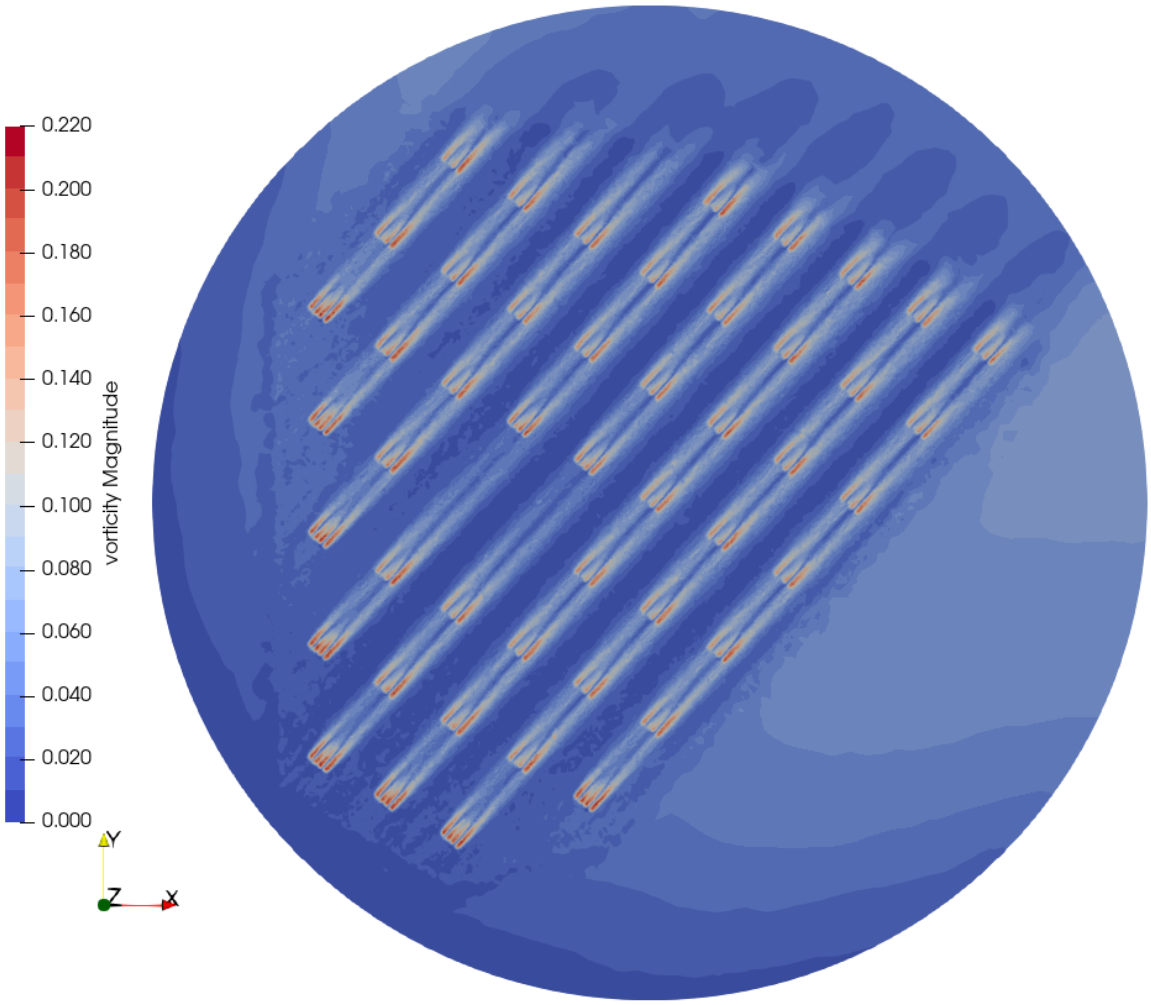

Figure 8: Instantaneous vorticity magnitude contours at the rotor hub height ($z = 65\ m$)

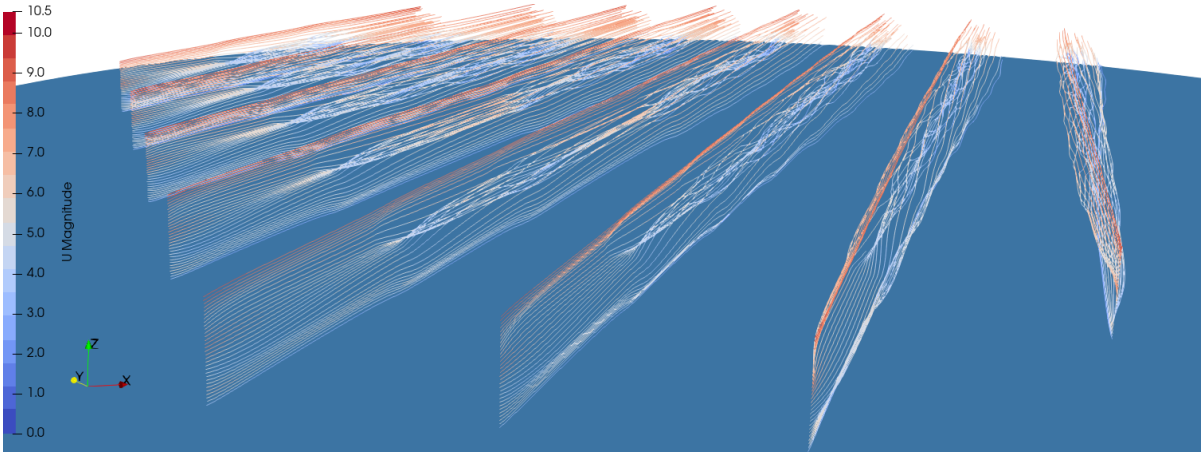

Figure 9: Instantaneous streamlines

row-second rotors, and recovers to $4.4\ m/s$ close to the downstream turbines. This trend remains almost constant at the further downstream turbines.

Vortices emanating from the blade tips of the row-first turbines show a similar structure at all rows,

retaining their shape all the way down to the row-second turbines (Fig. 8). Eddies are the strongest in the rotor vicinity, where the blade forces have their full effect in deflecting the velocity field. Wake recovery can also be observed here: as the flow travels downstream, vortices are reduced in magnitude. In addition to the blade tips, strong vortices can also be seen at the blade roots. This is due to the fact that the rotor hubs are not modeled in the present study. Thus, root vortices are present and a gap in the rotor centers are visible.

Both figures show an interesting outcome: if the center of the wake is traced visually, it can be seen that the wake is slightly deflected towards a certain direction. This is attributed to the rotation direction of the rotors, combined with the presence of the wall. In the simulation, all turbines rotate in the clockwise direction (when viewed from the upstream side). Accordingly, a swirling motion is induced to the flow in the opposite direction, as shown in Fig. 9. Streamlines indicate that the flow is rotated in the counter-clockwise direction behind each rotor. A close inspection of the row-second rotors in Fig. 7 reveals a higher velocity deficit at the right half of the rotors ($U = 3.7\ m/s$) compared to the left half ($U = 4.7\ m/s$). A similar difference in terms of vortex strength can be seen in Fig. 8, where the vortex magnitude is higher in the right hand side of the rotors.

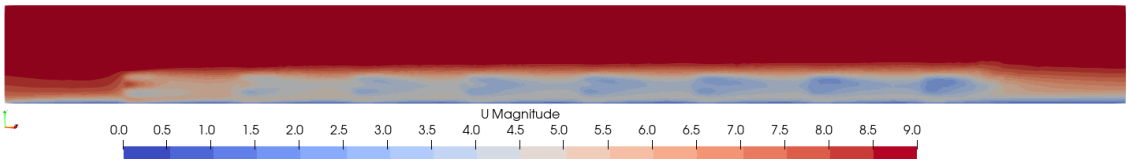

(a) Instantaneous velocity magnitude contours

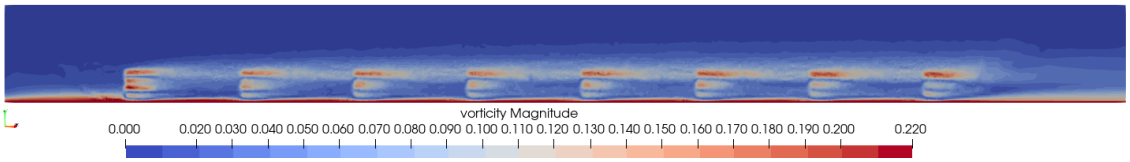

(b) Instantaneous vorticity magnitude contours

Figure 10: Vertical cuts passing through row B

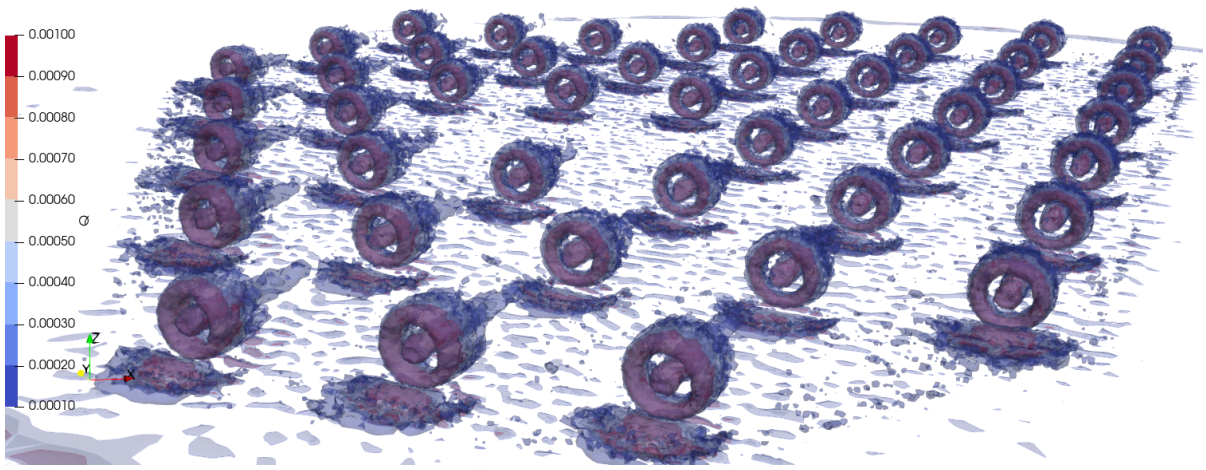

Figure 11: Instantaneous Q iso-surfaces (plotted levels: 0.0010, 0.0005 and $0.0002\ s^{-2}$)

Fig. 10 shows the vertical planar cuts passing through the rotor centers along row B. These cuts reveals the velocity and vorticity contours under the influence of the atmospheric boundary layer. The amount of deceleration in the flow increases after passing each turbine. Also, it is also notable that the eddy activity is higher in the upper half of the turbine. This is due to flow speed being higher at the upper end of the rotor, compared to its lower end.

Q criterion, defined as $Q = (||\Omega||^2 - ||S||^2)/2$, is a local measure of the excess rotation rate relative to the strain rate in an incompressible flow [Chakraborty et al., 2005]. The Q iso-surfaces are plotted in Fig. 11 shows the high rate of rotation in the rotor vicinity, especially around the blade tip and root circles. While the blade root eddies remain strong up to 2.5D downstream, eddies emanating from the blade tip die down around 1D downstream. It is a known fact that ADM falls short in terms of replicating tip vortices, compared to the ALM, which also shows in the current results.

The wake-induced power losses along each row (A-H) are presented in Fig. 12 and compared to the field measurements. Each turbine's power production is normalized with respect to the first turbine of the row, i.e. P/P_{first}. It should be noted that the ADM-R is implemented with a simple controller, that is, each turbine controls its rotor speed and blade pitch angle according to the monitored wind speed at its nacelle (rotor hub), and tracks maximum power (Fig. 5). In general, power loss at the row-second turbine is captured with high accuracy in all rows; where the field measurements show some average 36% loss, and the simulations results are around 40%. This is a high but expected power loss, due to the very tight turbine separation distance $(4.3D)$ and complete axial alignment. Some discrepancies are visible at the further downstream turbines. In row A, results show a consistent divergence from the SCADA data. The present study underpredicts the power loss by approximately 16% for the third and subsequent turbines. There a eight turbines in rows B and C, one more than in A. Some higher and lower power values are predicted at the second and third turbines, respectively. Interestingly, predictions become aligned with the last three turbines in these rows. Rows D and E have a single turbine gap behind the third and second turbines, respectively. The power deficit estimates for the first turbines following these gaps are in good agreement with the measured values. Rows F, G and H have lesser number of turbines, and the trend is similar to that of the previous rows.

These results indicate that the present study replicates the wake structures behind the row-first turbine accurately, which is subject to a uniform flow. But at the turbines that are under the influence of added turbulent activity from more than one rotors, results diverge from the measurements. This can be attributed to the turbulence closure model, as well as the design of the equivalent turbine. The velocity deficit in the wake is primarily affected by the thrust of the rotor, which is a function of the blade geometry and rotor speed. Design differences with the present turbine and the Siemens rotor is highly susceptible for such difference.

CONCLUSIONS

The Lillgrund offshore wind farm is simulated using the rotating actuator disk (ADM-R) and LES models. Since ADM-R requires the detailed blade geometry input, and it is not available for the Siemens rotors installed in the wind farm, an equivalent turbine is designed using Blade Element-Momentum (BEM) methodology. Unlike the uniformly-loaded ADM, the wake structures are captured with the swirling wake motion. Its effect on the slight wake deflection and non-uniform impact on the downstream rotors are observed. Power deficit results are in good agreement for the row-second turbines, whereas some discrepancies are present at the further downstream rotors. Primary reason for this is attributed to the equivalent rotor, whose thrust coefficient could not be compared to that of the Siemens rotor. As a future study, grid resolution, parameters of the Smagorinsky closure model, and moreover, the closure model itself will be further investigated.

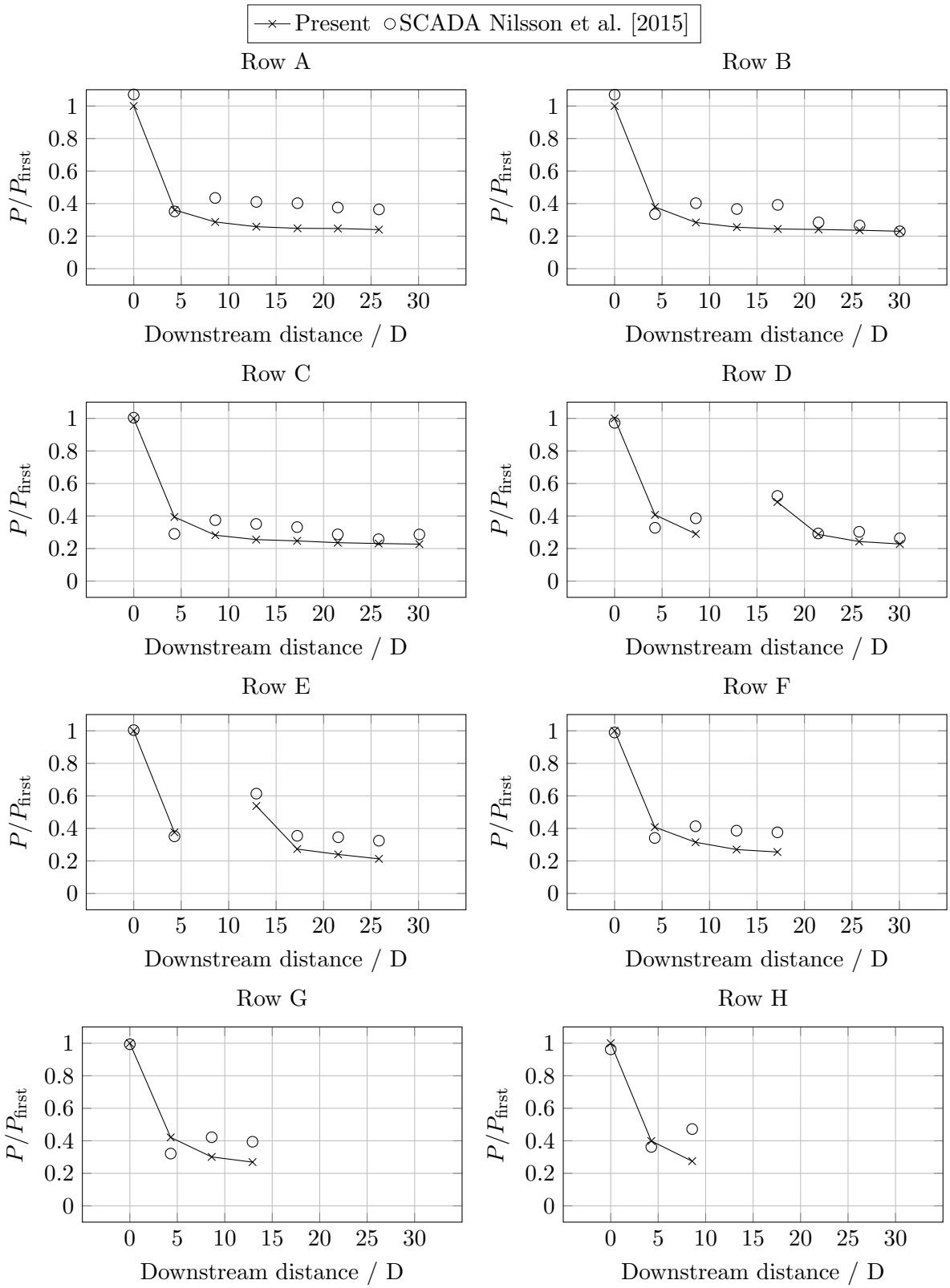

Figure 12: Relative rotor powers (P) normalized with respect to the row-first turbine. Downstream distance is shown per rotor diameter (D).

References

Barthelmie, R. J., Frandsen, S. T., Rathmann, O., Hansen, K., Politis, E. S., Prospathopoulos, J., Schepers, J. G., Rados, K., Cabezon, D., Schlez, W., Neubert, A., and Heath, M. (2011). Flow and Wakes in Large Wind Farms: Final Report for UPWIND WP8. (Risø-R-1765 (EN)).

Chakraborty, P., Balachandar, S., and Adrian, R. J. (2005). On the relationships between local vortex identification schemes. *Journal of Fluid Mechanics*, 535:189–214.

Churchfield, M. (2017). Simulator fOr Wind Farm Applications (SOWFA). Technical report, NREL, Ames, Iowa.

Churchfield, M. J., Lee, S., Moriarty, P. J., Martínez, L. A., Leonardi, S., Vijayakumar, G., and Brasseur, J. G. (2012). A large-eddy simulation of wind-plant aerodynamics. *50th AIAA Aerospace Sciences Meeting Including the New Horizons Forum and Aerospace Exposition*.

Drela, M. (1989). XFOIL: an analysis and design system for low Reynolds number airfoils. In *Low Reynolds Number Aerodynamics. Proc. Conf., Notre Dame, U.S.a., June 5-7, 1989 Edited By T.J. Mueller]. (Lecture Notes in*, number 54), Berlin, Germany, Springer-Verlag, 1989, pages 1–12. Springer Berlin Heidelberg.

Geuzaine, C. and Remacle, J. F. (2009). Gmsh: A 3-D finite element mesh generator with built-in pre- and post-processing facilities. *International Journal for Numerical Methods in Engineering*, 79(11):1309–1331.

Hargreaves, D. M. and Wright, N. G. (2007). On the use of the k-ϵlunate model in commercial CFD software to model the neutral atmospheric boundary layer. *Journal of Wind Engineering and Industrial Aerodynamics*, 95(5):355–369.

Internatonal Energy Agency (2023). Tracking Clean Energy Progress 2023.

Issa, R. I. (1986). Solution of the implicitly discretised fluid flow equations by operator-splitting. *Journal of Computational Physics*, 62(1):40–65.

Ivanell, S., Sørensen, J. N., and Henningson, D. (2007). *Numerical Computations of Wind Turbine Wakes*. PhD thesis, KTH.

Jeppsson, J., Larsen, P. E., and Larsson, A. (2008). Technical Description Lillgrund Wind Power Plant. *Vattenfall Vindkraft AB*, (September):79.

Jonkman, J., Butterfield, S., Musial, W., and Scott, G. (2009). Definition of a 5-MW reference wind turbine for offshore system development. *Contract*, (February):1–75.

Marten, D. and Wendler, J. (2013). QBLADE: an open source tool for design and simulation of horizontal and vertical axis wind turbines. *International Journal of Emerging Technology and Advanced Engineering*, 3(3):264–269.

Martínez, L. A., Leonardi, S., Churchfield, M. J., and Moriarty, P. J. (2012). A comparison of actuator disk and actuator line wind turbine models and best practices for their use. In *50th AIAA Aerospace Sciences Meeting Including the New Horizons Forum and Aerospace Exposition*.

Martínez-Tossas, L. A., Branlard, E., Shaler, K., Vijayakumar, G., Ananthan, S., Sakievich, P., and Jonkman, J. (2022). Numerical investigation of wind turbine wakes under high thrust coefficient. *Wind Energy*, 25(4):605–617.

Nilsson, K., Ivanell, S., Hansen, K. S., Mikkelsen, R., Sørensen, J. N., Breton, S. P., and Henningson, D. (2015). Large-eddy simulations of the Lillgrund wind farm. *Wind Energy*, 18(3):449–467.

Olivares-Espinosa, H., Breton, S. P., Masson, C., and Dufresne, L. (2014). Turbulence characteristics in a free wake of an actuator disk: Comparisons between a rotating and a non-rotating actuator disk in uniform inflow. *Journal of Physics: Conference Series*, 555(1):12081.

Porté-Agel, F., Wu, Y. T., Lu, H., and Conzemius, R. J. (2011). Large-eddy simulation of atmospheric boundary layer flow through wind turbines and wind farms. In *Journal of Wind Engineering and Industrial Aerodynamics*, volume 99, pages 154–168.

qi Wang, S., Xu, G., qing Zhu, R., and Wang, K. (2018). Hydrodynamic analysis of vertical-axis tidal current turbine with surging and yawing coupled motions. *Ocean Engineering*, 155:42–54.

SMAGORINSKY, J. (1963). General Circulation Experiments With the Primitive Equations. *Monthly Weather Review*, 91(3):99–164.

Sohoni, V., Gupta, S. C., and Nema, R. K. (2016). A Critical Review on Wind Turbine Power Curve Modelling Techniques and Their Applications in Wind Based Energy Systems. *Journal of Energy*, 2016:1–18.

Sørensen, J. N. and Shen, W. Z. (2002). Numerical modeling of wind turbine wakes. *Journal of Fluids Engineering, Transactions of the ASME*, 124(2):393–399.

Stevens, R. J., Martínez-Tossas, L. A., and Meneveau, C. (2018). Comparison of wind farm large eddy simulations using actuator disk and actuator line models with wind tunnel experiments. *Renewable Energy*, 116:470–478.

Tabib, M., Rasheed, A., and Kvamsdal, T. (2015). LES and RANS simulation of onshore Bessaker wind farm: Analysing terrain and wake effects on wind farm performance. *Journal of Physics: Conference Series*, 625(1):12032.

Van Der Laan, M. P., Sørensen, N. N., Réthoré, P. E., Mann, J., Kelly, M. C., Troldborg, N., Hansen, K. S., and Murcia, J. P. (2015). The k- ϵ -fP model applied to wind farms. *Wind Energy*, 18(12):2065–2084.

Weller, H. G., Tabor, G., Jasak, H., and Fureby, C. (1998). A tensorial approach to computational continuum mechanics using object-oriented techniques. *Computers in Physics*, 12(6):620.

Wu, Y. T. and Porté-Agel, F. (2011). Large-Eddy Simulation of Wind-Turbine Wakes: Evaluation of Turbine Parametrisations. *Boundary-Layer Meteorology*, 138(3):345–366.